Draft 2/3/20 AZ

Electron Beam-Induced Nanopores in Bernal-Stacked Hexagonal Boron Nitride

Mehmet Dogan[1,2 (*)], Matt Gilbert[1,2,3 (*)], Thang Pham[1,2,3,4], Brian Shevitski[1,3,5], Peter Ercius[5], Shaul Aloni[5], Alex Zettl[1,2,3,#], Marvin L. Cohen[1,2,#]

[1] Department of Physics, University of California, Berkeley, CA 94720, USA
[2] Materials Sciences Division, Lawrence Berkeley National Laboratory, Berkeley, CA 94720, USA
[3] Kavli Energy NanoScience Institute at the University of California, Berkeley, and the Lawrence Berkeley National Laboratory, Berkeley, CA 94720, USA
[4] Department of Materials Science and Engineering, University of California, Berkeley, CA 94720, USA
[5] Molecular Foundry, Lawrence Berkeley National Laboratory, Berkeley, CA 94720, USA
[(*)] These authors contributed equally to this work.
[(#)] To whom correspondence should be addressed: azettl@berkeley.edu, mlcohen@berkeley.edu

Abstract

Controlling the size and shape of nanopores in two-dimensional materials is a key challenge in applications such as DNA sequencing, sieving, and quantum emission in artificial atoms. We here investigate experimentally and theoretically triangular vacancies in (unconventional) Bernal-stacked AB-*h*-BN formed using a high-energy electron beam. Due to the geometric configuration of AB-*h*-BN, triangular pores in different layers are aligned, and their sizes are controlled by the duration of the electron irradiation. Interlayer covalent bonding at the vacancy edge is not favored, as opposed to what occurs in the more common AA′-stacked BN. A variety of monolayer and bilayer pores in bilayer AB-*h*-BN are observed in high-resolution transmission electron microscopy and characterized using *ab initio* simulations. Bilayer pores in AB-*h*-BN are commonly formed, and grow without breaking the bilayer character. Nanopores in AB-*h*-BN exhibit a wide range of electronic properties, ranging from half-metallic to semiconducting, indicating that, in addition to the pore size, the electronic structure is also highly controllable in these systems and can potentially be tuned for particular applications.

Introduction

Vacancy defects in two-dimensional materials are zero-dimensional features that can impart to the host material optical and electronic properties (e.g. bandgaps, charge state, and electron scattering behavior) very different from those of the host pristine sheets, and they can change the emergent measurable properties of the material (e.g. resistivity and tensile strength).[1–5] Moreover, such vacancies represent a physical structure in which there may be a small hole (i.e. nanopore) in an otherwise impermeable membrane.

Simultaneous advances in atomic resolution transmission electron microscopy (TEM) and in the isolation and large-scale synthesis of two dimensional materials have resulted in a rapid increase in the understanding of vacancy defects in these materials.[6–8] These vacancies have been studied in both naturally occurring and artificially produced forms, and they have been structurally characterized.[2,9–13] The fundamental properties of vacancy defects in two-dimensional materials

have led to their investigation in numerous research directions, including (i) *DNA Sequencing*, in which the DNA is pushed through a pore in a solution while the ionic current across the pore, which is a function of the nucleotide base currently inside the pore, is continuously measured;[14–19] (ii) *Quantum Emission*, in which pores behave as artificial atoms or quantum dots with stable and optically accessible quantum states with long coherence times at room temperature;[20] and (iii) *Molecular Sieving*, in which the size distribution of a large number of pores in an impermeable membrane is controlled to selectively exclude the passage of certain molecules or ions.[21–26]

For these applications, vacancy size and geometry are critical for determining the utility of nanopores. While high energy electron beams and ion beams have been used to create the smallest pores observed, the shape and size of nanopores is limited by the beam geometry.[11,17,27] For graphene nanopores, for example, pore size has traditionally been limited to 3 nm or greater and their shapes can only be minimally controlled.[17] In order to overcome this minimum resolution limit, the intrinsic etching properties of the material can be leveraged. It has been demonstrated that when conventionally AA'-stacked hexagonal boron nitride (AA'-*h*-BN) is exposed to 80 kV electron irradiation in TEM, vacancies are etched, and atomically precise edges are formed along the nitrogen zig-zag direction.[6,12,28–32]

In single-layer *h*-BN, single atomic vacancies are preferentially formed as boron monovacancies under a 80 kV electron beam, which is generally thought to be caused by the difference in the electron knock-on energy thresholds of boron and nitrogen atoms (74 kV for B and 84 kV for N).[10,12,28,33,34] The computed atomic structure of a boron monovacancy is shown in **Figure 1a**, which results in a half-metallic electronic structure, where one spin channel has a bandgap and the other has a non-zero density of states at the Fermi level. After the formation of a B monovacancy, under continuing electron irradiation, one of the under-coordinated nitrogen atoms adjacent to the vacancy gets ejected, followed by its neighboring boron atoms, which results in a triangular tetravacancy with a nitrogen edge. Maintaining the electron irradiation further results in progressively larger triangular vacancies.[32,35] This mechanism provides a method of creating nanopores that are equilateral triangles with the desired sizes by controlling the duration of the irradiation. According to previous computational studies, the electronic structure of these triangular pores depends on their size, resulting in metallic, half-metallic or semiconducting edge regions.[36–40] Because single layer *h*-BN is rarely observed in large-area free-standing form, it would be beneficial to have the same level of control on the triangular vacancies in multilayer samples. In this Letter, we describe how this is achieved, and characterize the electronic properties of these vacancies using first-principles calculations.

Monolayer Vacancies in Bilayer *h*-BN

In multilayer *h*-BN, the vacancy defects can interact with adjacent layers.[3,4] This can affect the types and shapes of vacancies in the sheets. For example, in AA′-stacked *h*-BN, interlayer interactions can dominate the properties of its electron irradiation induced defects. Out-of-plane covalent bonds form across layers at boron monovacancy sites in bilayers.[3] Also, along the edges of extended vacancies in these bilayers, covalent bonds form between the layers and the edge relaxes to resemble a boron nitride nanotube with an extremely small radius of curvature.[4] The

local atomic structure at these defects and edges determines the electronic properties of the material.[3,4]

Each lattice site in AA′-stacked *h*-BN contains a boron directly under a nitrogen, thus interlayer covalent bonds are available at each site in the crystal. When a B monovacancy is formed, some or all of the three under-coordinated N atoms neighboring the vacancy may form bonds with the B atoms directly underneath (see **Figure 1b**). We find that in the electron-rich regime (3 extra electrons per 5×5 cell), forming these interlayer bonds is energetically favorable, with 2 out of 3 bonds being the most favorable configuration (see **Table 1**). Therefore, the vacancy shape is no longer determined, and the three-fold rotational symmetry of the lattice may be lost. These lower-symmetry defects have been observed in AA′-stacked *h*-BN.[3] When all 3 of the interlayer bonds are formed, the vacancy becomes a semiconductor, losing the half-metallic character of the B monovacancy edge (compare **Figure 1b** with **Figure 1a**). Furthermore, in the AA′-stacked BN, the second layer is obtained from the first layer by a 60° rotation, thus the triangular pores with N edge in successive layers are not aligned, and multilayer pores do not have a pre-determined shape (see **Figure S1**). This is consistent with the observations in References [6,12,28].

In Reference [35], we described a new synthesis technique for reliably producing Bernal-stacked *h*-BN, i.e. AB-*h*-BN. For this stacking sequence, the relative shift between the layers leaves only half of the lattice sites with a stacked boron and nitrogen. In **Figure 1c-d**, we present the structure of a boron monovacancy in one layer of double layer AB-*h*-BN. As opposed to the AA′ stacking, in AB-*h*-BN the two layers are inequivalent: in **Figure 1c**, the B atoms in the top layer are aligned with the hollow sites in the bottom layer, whereas the B atoms in the bottom layer are aligned with the N atoms in the top layer. Thus, a vacancy in the top layer yields a different configuration from a vacancy in the bottom layer. In order to consider vacancies only in the top layer, we flip the system over if the vacancy is in the bottom layer, and give it a different name (AB1 for **Figure 1c** and AB2 for **Figure 1d**). The two stacking sequences are physically equivalent, and any vacancy configuration in one can be obtained in the other by rotating the system by 180° around an armchair direction. Distinguishing AB1 and AB2 allows us to meaningfully distinguish a top layer and a bottom layer in the discussion below.

In AB1 stacking, a B monovacancy in the top layer creates three under-coordinated N atoms that are directly on top of B atoms from the bottom layer, which yields interlayer bonding in the electron-rich regime, as in the AA′ case (see **Figure 1c** and **Table 1**). However, in the AB2 stacking, the under-coordinated N atoms lack a neighbor directly underneath, and thus the top layer stays flat and no new bonds form (see **Figure 1d**). Decoupling the two layers retains the half-metallic nature of the B monovacancy in the top layer (**Figure 1d**). Furthermore, in the Bernal stacking, because there is no relative rotation between layers,[35] the triangular pores with N edge in successive layers are aligned and multilayer triangular pores are formed (see **Figure S1**). Moreover, the edges of each vacancy are nearly straight, and we do not observe any irregular shaped vacancies.

Studying our AB-*h*-BN samples using high-resolution transmission electron microscopy (HR-TEM), we find many monolayer vacancies in two-layer stacks. **Figure 2** shows three such monolayer vacancies as imaged in HR-TEM and modelled theoretically. Assuming that the pores are formed in the top layer, the first one corresponds to AB2 stacking with a boron monovacancy

(**Figure 2a**). In the second one, a tetravacancy is formed in the top layer of an AB1 bilayer (**Figure 2b**). The third one corresponds to a larger nanopore with 10 B and 6 N atoms missing from the top layer in a bilayer AB2-stacked BN. The relaxed theoretical structures (which contain no interlayer covalent bonds) match the experimental HR-TEM structure almost exactly, as shown in the middle row. Spin-resolved density-functional calculations result in three distinct characterizations for these vacancies: The first one is a half-metal with a total magnetization of 3 μ_B (**Figure 2a**); the second one is a non-magnetic semiconductor with two sharp in-gap states 1.8 eV and 2.2 eV above the valence band maximum (**Figure 2b**); and the third one is a magnetic semiconductor with gaps of 0.6 eV and 0.2 eV for the two spin channels and a total magnetization of 6 μ_B (**Figure 2c**). This result suggests that tuning vacancy size in AB-*h*-BN is a new method for tuning the magnetic and electronic properties of its vacancies. The ability to create vacancies with tunable bandgaps in the visible range may be useful for *h*-BN in optoelectronics and photon emission.[20,41]

Bilayer Vacancies and Edges in Bilayer *h*-BN

In a multilayer sample, after a monolayer triangular vacancy is formed, if the electron irradiation is maintained, a triangular vacancy tends to form in the exposed region of the other layer, resulting in nested triangular vacancies. **Figure S2** shows the growth of a vacancy in a monolayer of *h*-BN as it merges with a larger vacancy in the next layer to form a bilayer AB-*h*-BN nanopore. In panel (a) of **Figure S2**, a small one- or few-atom vacancy has formed within a triangular monolayer region that is embedded within a bilayer area (~2 nm triangle). By panel (b), the vacancy has grown to ~1.5 nm and two of its edges have aligned with the large vacancy to form bilayer edges. In panel (c), the vacancy in the two layers have merged to form a ~4 nm triangular bilayer vacancy. In panel (d), the triangular bilayer vacancy has grown to ~6 nm while retaining its bilayer edges and triangular geometry. Typically, these bilayer edges keep their triangular shape and bilayer edges as they continue to grow, and never revert to two separate monolayers.

While the interlayer orientation is sufficient to describe the alignment of vacancies in multiple layers, it does not fully explain why the vacancies should merge to preferentially form a bilayer edge. We suggest two mechanism by which bilayer edges emerge. The first possible mechanism is that bare monolayers of *h*-BN are less stable under electron irradiation. This could be because a second layer provides protection from chemical sputtering from the electron beam or because the second layer increases the kinetic scattering threshold for the layers among other reasons. In this scenario, whenever a small monolayer region of *h*-BN is exposed, the layer is etched back to form a bilayer edge. The second possible mechanism is that a covalent bond forms between the edge atoms. In this scenario, as the triangular vacancies in the top and bottom *h*-BN layers intersect, the edge atoms covalently bond together. This would form a stable edge that maintains its structure as it is irradiated and reforms as it is etched. These two mechanisms can be distinguished by their structural properties as in Reference [4].

In order to understand the structure of its edges, we performed HR-TEM on vacancies in bilayer AB-*h*-BN using the TEAM 0.5 microscope at Lawrence Berkeley National Laboratory. Figure 3.6 shows the exit wave reconstruction (mac tempas) of a focal series stack (-10 nm to 70 nm) of

80 monochromated TEM images acquired at 80 kV. The image is presented using a high-contrast filter to distinguish between vacuum (black and dim red), single atoms (bright red dots), and stacks of B and N atoms (yellow dots).

Figure 3a shows an overview of two 3 nm bilayer vacancies in the AB stacked *h*-BN as highlighted by the green triangles. Multiple smaller monolayer vacancies are also present. The edge highlighted by the blue dashed box is presented in **Figure 3b**. An overlaid grid denotes spacings of half the interatomic distance ($a_0/2$) in the *y*-direction and $\sqrt{3}a_0/2$ in the *x*-direction; all of the atomic positions for the undisturbed lattice fall on this grid, as shown in **Figure 3c**. We observe that each double atom stack of boron and nitrogen falls exactly on the grid of the undisturbed lattice, independent of how close they fall to the edge. This indicates that interlayer relaxation and covalent bond formation is unlikely in these bilayer edges.

To further understand the properties of the edges of the Bernal-stacked bilayer vacancies, we computed possible edge structures. The best candidate for the bilayer edge in **Figure 3** is presented in **Figure 4**. In this "open edge" case, two monolayer edges sit on top of one another without interlayer bonding. Other candidates for bilayer edges, including some "closed edge" cases will be presented elsewhere. The unrelaxed grid of positions is overlaid on the open edge structure as in **Figure 3**. The in-plane distortions are negligible, making it a very strong candidate for the experimentally observed bilayer edge. In previous computational studies, the nitrogen-terminated zigzag edge of the BN monolayer was found to be half-metallic.[36,42] Looking at the projected density of states (PDOS) plots in **Figure 4**, we see that the open bilayer edge preserves the half-metallic character of the monolayer edge, with a magnetization of 2 μ_B per cell along the edge direction, localized on the edge N atoms.

Therefore, bilayer edges in AB-*h*-BN greatly differ from the bilayer edges in AA′-stacked BN, which are insulating and have large in-plane and out-of-plane relaxations.[4] This is an important difference as it suggests that AB-*h*-BN could potentially be used for its 1D conducting edges. Also, the formation of bilayer edges in AA′-stacked *h*-BN occurs because of stabilizing interlayer bonds, but the formation of bilayer edges in AB-*h*-BN (where the edges in the consecutive layers are not bonded but are nevertheless aligned) appears to be a kinetic effect. This highlights that both the roles of the chemistry in the TEM column and knock-on effects have major roles in determining defect geometry in materials.

Conclusions

We have achieved the controlled formation of triangular vacancies in multilayer *h*-BN, using a new growth technique which results in Bernal stacking (AB-*h*-BN). Due to the favorability of nitrogen terminated vacancy edges in BN and the lack of relative rotation between the layers in Bernal stacking, triangular pores in different layers are aligned in AB-*h*-BN. We have shown that interlayer covalent bonding following vacancy formation in a layer is not favored for this stacking sequence, increasing the level of controllability and symmetry in these pores. Furthermore, we observe that pores with bilayer edges are preferentially formed, which is probably not due to interlayer covalent bonds but kinetic effects. We observe a variety of monolayer and bilayer pores in bilayer BN in our HR-TEM images and find excellent matches

from theoretical simulations. These pores have a variety of electronic properties, ranging from half-metallic to semiconducting, which is encouraging for future research toward many applications such as DNA sequencing and quantum dots.

Methods

We use low-pressure chemical vapor deposition (LP-CVD) on Cu and Fe surfaces to grow Bernal-stacked *h*-BN. We verify the Bernal-stacking of the resulting multilayer flakes using high-resolution transmission electron microscopy (HR-TEM) and selected area electron diffraction (SAED). We employ a two-zone heating approach in which the gaseous thermal decomposition products of solid ammonia-borane (heated at 70 °C–90 °C) react to form h-BN on a transition metal catalyst (heated at 1025 °C). HR-TEM was carried out at 80 kV using the TEAM 0.5 microscope with spherical aberration correction. The growth and characterization procedures were described in great detail in Reference [35] and its Supplementary Material. **[Matt: please edit and complete]**

We employ density functional theory (DFT) in the Perdew–Burke–Ernzerhof generalized gradient approximation (PBE GGA) to conduct the first-principles calculations.[43] We implement DFT using the QUANTUM ESPRESSO software package with norm-conserving pseudopotentials.[44,45] We set 160 Ry as the plane-wave energy cutoff for the pseudo Kohn-Sham wavefunctions. For single- and double-layer simulations, we use a 12×12×1 Monkhorst-Pack k-point mesh to sample the Brillouin zone. For edge simulations, we use a 12×1×1 k-point mesh. All atomic coordinates are relaxed until the forces on all the atoms are less than 10^{-3} Ry/a_0 in all three Cartesian directions (a_0: Bohr radius). A ~14 Å thick vacuum is used between the periodic copies of the slab in the out-of-plane direction. For edge simulations, a 1×10 cell is constructed, and ~12 Å of vacuum is placed between the copies of the 1D system along the direction perpendicular to the edge. We passivate the dangling bonds at the other edge, which is not of interest to us, using hydrogen atoms, and keep the first 4 unit cells (8 atoms) unrelaxed. In order to include the interlayer van der Waals (vdW) interactions, we include a Grimme-type dispersion correction.[46]

Acknowledgements

This work was supported primarily by the Director, Office of Science, Office of Basic Energy Sciences, Materials Sciences and Engineering Division, of the U.S. Department of Energy under contract No. DE-AC02-05-CH11231, within the sp2-bonded Materials Program (KC2207), which supported TEM imaging and XXX computations. Sample growth was supported by the Director, Office of Science, Office of Basic Energy Sciences, Materials Sciences and Engineering Division, of the U.S. Department of Energy under contract No. DE-AC02-05-CH11231, within the Van der Waals Heterostructures Program (KCWF16) which supported sample growth. Further support for theoretical work was provided by the NSF Grant No. DMR-1926004 which supported XXX computations. Computational resources were provided by the DOE at Lawrence Berkeley National Laboratory's NERSC facility and the NSF through XSEDE resources at NICS. We thank Sehoon Oh for fruitful scientific discussions.

Table 1. Energies of the interlayer-bonded structures for boron monovacancies. Energies of the interlayer-bonded structures, relative to the configuration in which out-of-plane relaxations are not allowed, for the boron monovacancy in one layer of a bilayer AA′-stacked and AB1-stacked *h*-BN. The calculations are carried out in electron-rich conditions (3 extra electrons per 5×5 cell), following Reference [3]. For each stacking sequence, formation of 1, 2 or 3 interlayer bonds is possible between the pairs of N atoms at the edge of the vacancy in the top layer and the B atoms directly underneath; so each case corresponds to a (meta)stable configuration.

	ΔE (eV)		
	1 IL bond	**2 IL bonds**	**3 IL bonds**
AA′	-1.09	-1.49	-1.08
AB1	-1.03	-1.36	-1.07

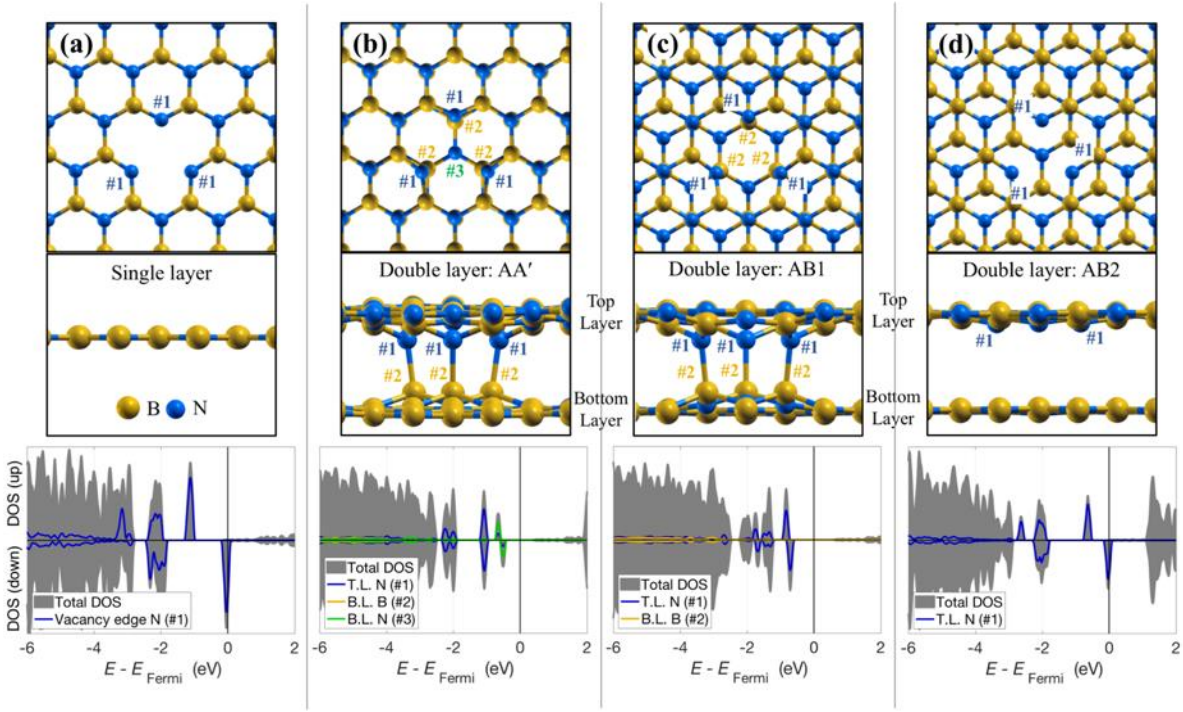

Figure 1. Simulated boron monovacancies in monolayer and bilayer *h*-BN. Relaxed atomic structure and density of states (DOS) of a boron monovacancy in (a) monolayer, (b) AA′-stacked bilayer, (c) AB1-stacked bilayer and (d) AB2-stacked bilayer *h*-BN. For each structure, top and side views of the atomic configuration are presented at the top. The calculations are carried out in electron-rich conditions (3 extra electrons per 5×5 cell), following Reference [3]. Boron is shown in gold and nitrogen is shown in blue. Computed spin-resolved density of states (DOS) plots for each structure are presented at the bottom. The total DOS is plotted as gray areas, and the colored curves are obtained by adding up the DOS projected onto the 2s and 2p orbitals (PDOS) of the atoms marked on the figure: (a) 3 edge N atoms (blue); (b) 3 edge N atoms in the top layer (blue), 3 B atoms directly underneath (gold), 1 N atom in the bottom layer directly under the vacancy (green); (c) 3 edge N atoms in the top layer (blue), 3 B atoms directly underneath (gold); (d) 3 edge N atoms in the top layer (blue).

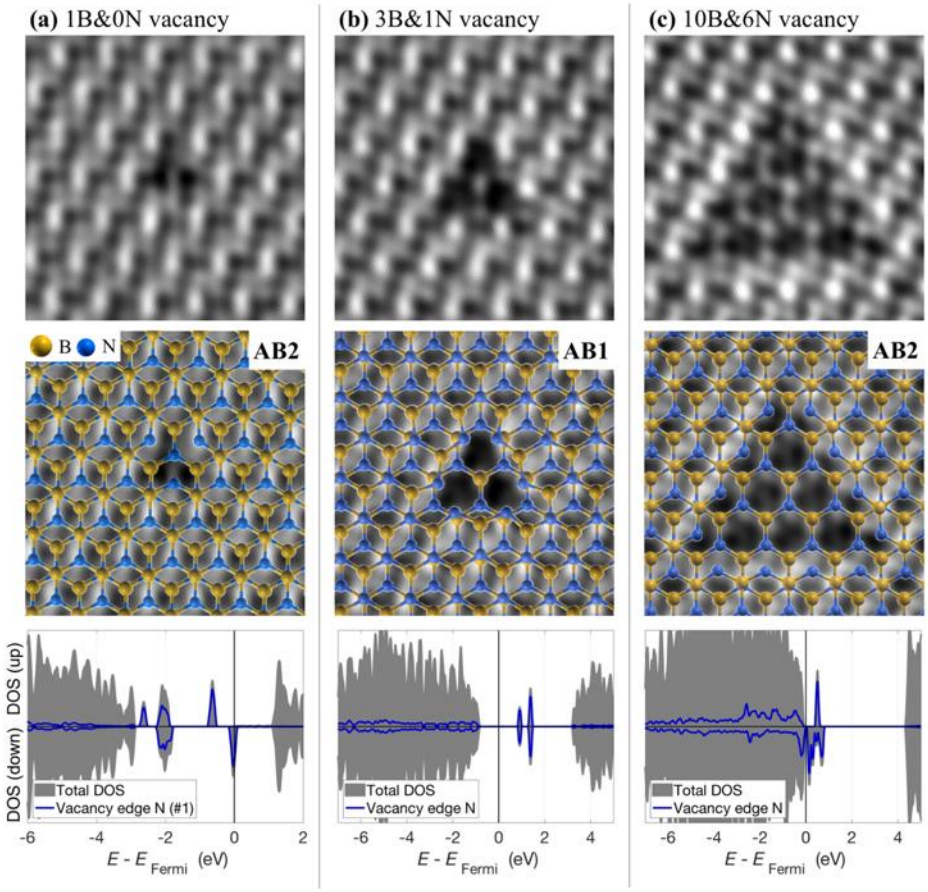

Figure 2. Vacancies in one layer of a bilayer Bernal-stacked h-BN. Top row: HR-TEM focal series reconstructions of vacancies produced in a single layer of a bilayer AB-stacked h-BN, comprised of (a) 1 missing boron atom (monovacancy), (b) 3 missing boron atoms and 1 missing nitrogen atom (tetravacancy), and (c) 10 missing boron atoms and 6 missing nitrogen atoms. The frames are each 2 nm wide. Middle row: Same images with the computed atomic structures overlaid. Boron is shown in gold and nitrogen is shown in blue. The relaxed theoretical structures (which contain no interlayer covalent bonds) match the experimental HR-TEM structure almost exactly. Bottom row: Computed spin-resolved density of states (DOS) plots for each structure. The total DOS is plotted as gray areas, and the blue curves are obtained by adding up the DOS projected onto the 2s and 2p orbitals (PDOS) of the under-coordinated N atoms at the vacancy edges. The structure in (a) is a half-metal, the structure in (b) is a non-magnetic semiconductor, and the structure in (c) is a magnetic semiconductor.

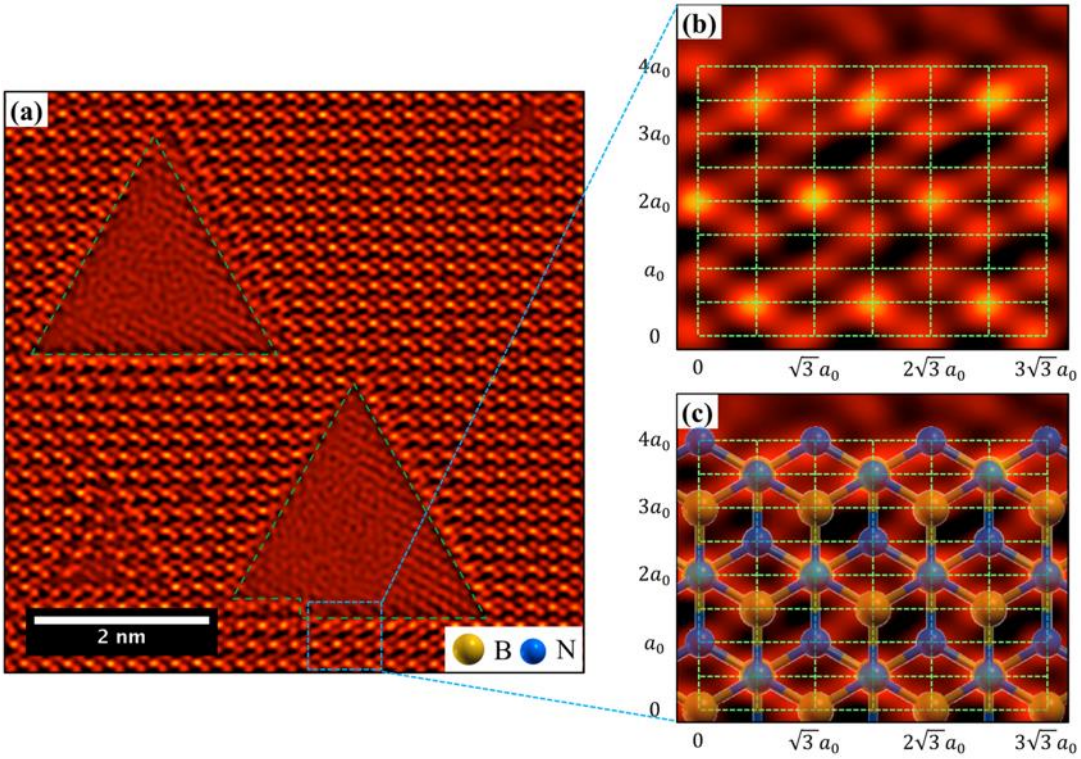

Figure 3. HR-TEM of triangular vacancies in Bernal-stacked h-BN. (a) Triangular vacancies produced in h-BN under 80 kV electron irradiation using TEM mode on the National Center for Electron Microscopy's TEAM 0.5. Two 3 nm bilayer pores (highlighted in green) are present with several smaller monolayer vacancies. The image is presented using a high-contrast filter to distinguish between vacuum (black and dim red), single boron and atoms (bright red dots), and stacks of boron and nitrogen (yellow dots). (b) A zoomed in section of the edge highlighted by blue dashed box in (a). An overlaid grid denotes the atomic positions for the undisturbed bilayer *h*-BN lattice. (c) The same zoomed in section of the edge from (a) with the atomic species in an undisturbed lattice overlaid. Boron is shown in gold and nitrogen is shown in blue.

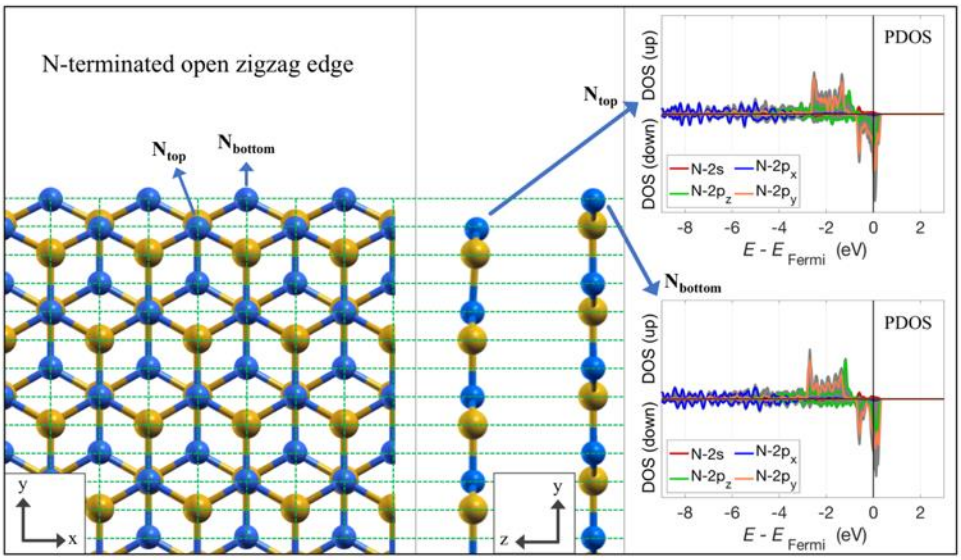

Figure 4. Simulated edge structure and electronic structure in Bernal-stacked bilayer *h*-BN. The nitrogen-terminated open zigzag edge, which exhibits no in-plane compression and its projected density of states (PDOS) for the edge atoms. The top view (left) and the side view (center) of the edge are shown, along with the PDOS of the atoms at the very edge (right). For the atomic models, an overlaid grid denotes the atomic positions for the undisturbed bilayer *h*-BN lattice, highlighting where the atoms would be if no relaxations due to the edge were allowed. Boron is shown in gold and nitrogen is shown in blue.

References

(1) Iberi, V.; Liang, L.; Ievlev, A. V.; Stanford, M. G.; Lin, M.-W.; Li, X.; Mahjouri-Samani, M.; Jesse, S.; Sumpter, B. G.; Kalinin, S. V.; et al. Nanoforging Single Layer MoSe 2 Through Defect Engineering with Focused Helium Ion Beams. *Scientific Reports* **2016**, *6* (1), 1–9. https://doi.org/10.1038/srep30481.

(2) Chen, J.-H.; Autès, G.; Alem, N.; Gargiulo, F.; Gautam, A.; Linck, M.; Kisielowski, C.; Yazyev, O. V.; Louie, S. G.; Zettl, A. Controlled Growth of a Line Defect in Graphene and Implications for Gate-Tunable Valley Filtering. *Phys. Rev. B* **2014**, *89* (12), 121407. https://doi.org/10.1103/PhysRevB.89.121407.

(3) Alem, N.; Yazyev, O. V.; Kisielowski, C.; Denes, P.; Dahmen, U.; Hartel, P.; Haider, M.; Bischoff, M.; Jiang, B.; Louie, S. G.; et al. Probing the Out-of-Plane Distortion of Single Point Defects in Atomically Thin Hexagonal Boron Nitride at the Picometer Scale. *Phys. Rev. Lett.* **2011**, *106* (12), 126102. https://doi.org/10.1103/PhysRevLett.106.126102.

(4) Alem, N.; Ramasse, Q. M.; Seabourne, C. R.; Yazyev, O. V.; Erickson, K.; Sarahan, M. C.; Kisielowski, C.; Scott, A. J.; Louie, S. G.; Zettl, A. Subangstrom Edge Relaxations Probed by Electron Microscopy in Hexagonal Boron Nitride. *Phys. Rev. Lett.* **2012**, *109* (20), 205502. https://doi.org/10.1103/PhysRevLett.109.205502.

(5) Halbertal, D.; Shalom, M. B.; Uri, A.; Bagani, K.; Meltzer, A. Y.; Marcus, I.; Myasoedov, Y.; Birkbeck, J.; Levitov, L. S.; Geim, A. K.; et al. Imaging Resonant Dissipation from Individual Atomic Defects in Graphene. *Science* **2017**, *358* (6368), 1303–1306. https://doi.org/10.1126/science.aan0877.

(6) Alem, N.; Erni, R.; Kisielowski, C.; Rossell, M. D.; Gannett, W.; Zettl, A. Atomically Thin Hexagonal Boron Nitride Probed by Ultrahigh-Resolution Transmission Electron Microscopy. *Phys. Rev. B* **2009**, *80* (15), 155425. https://doi.org/10.1103/PhysRevB.80.155425.

(7) Rasool, H. I.; Ophus, C.; Zettl, A. Atomic Defects in Two Dimensional Materials. *Advanced Materials* **2015**, *27* (38), 5771–5777. https://doi.org/10.1002/adma.201500231.

(8) Girit, Ç. Ö.; Meyer, J. C.; Erni, R.; Rossell, M. D.; Kisielowski, C.; Yang, L.; Park, C.-H.; Crommie, M. F.; Cohen, M. L.; Louie, S. G.; et al. Graphene at the Edge: Stability and Dynamics. *Science* **2009**, *323* (5922), 1705–1708. https://doi.org/10.1126/science.1166999.

(9) Pham, T.; P. Goldstein, A.; P. Lewicki, J.; O. Kucheyev, S.; Wang, C.; P. Russell, T.; A. Worsley, M.; Woo, L.; Mickelson, W.; Zettl, A. Nanoscale Structure and Superhydrophobicity of Sp 2 - Bonded Boron Nitride Aerogels. *Nanoscale* **2015**, *7* (23), 10449–10458. https://doi.org/10.1039/C5NR01672J.

(10) Alem, N.; Erni, R.; Kisielowski, C.; Rossell, M. D.; Hartel, P.; Jiang, B.; Gannett, W.; Zettl, A. Vacancy Growth and Migration Dynamics in Atomically Thin Hexagonal Boron Nitride under Electron Beam Irradiation. *Physica Status Solidi – Rapid Research Letters* **2011**, *5* (8), 295–297. https://doi.org/10.1002/pssr.201105262.

(11) Robertson, A. W.; Lee, G.-D.; He, K.; Gong, C.; Chen, Q.; Yoon, E.; Kirkland, A. I.; Warner, J. H. Atomic Structure of Graphene Subnanometer Pores. *ACS Nano* **2015**, *9* (12), 11599–11607. https://doi.org/10.1021/acsnano.5b05700.

(12) Meyer, J. C.; Chuvilin, A.; Algara-Siller, G.; Biskupek, J.; Kaiser, U. Selective Sputtering and Atomic Resolution Imaging of Atomically Thin Boron Nitride Membranes. *Nano Lett.* **2009**, *9* (7), 2683–2689. https://doi.org/10.1021/nl9011497.

(13) Gibb, A. L.; Alem, N.; Chen, J.-H.; Erickson, K. J.; Ciston, J.; Gautam, A.; Linck, M.; Zettl, A. Atomic Resolution Imaging of Grain Boundary Defects in Monolayer Chemical Vapor Deposition-Grown Hexagonal Boron Nitride. *J. Am. Chem. Soc.* **2013**, *135* (18), 6758–6761. https://doi.org/10.1021/ja400637n.

(14) Heerema, S. J.; Dekker, C. Graphene Nanodevices for DNA Sequencing. *Nature Nanotechnology* **2016**, *11* (2), 127–136. https://doi.org/10.1038/nnano.2015.307.

(15) Deamer, D.; Akeson, M.; Branton, D. Three Decades of Nanopore Sequencing. *Nature Biotechnology* **2016**, *34* (5), 518–524. https://doi.org/10.1038/nbt.3423.
(16) Haynes, T.; Smith, I. P. S.; Wallace, E. J.; Trick, J. L.; Sansom, M. S. P.; Khalid, S. Electric-Field-Driven Translocation of SsDNA through Hydrophobic Nanopores. *ACS Nano* **2018**, *12* (8), 8208–8213. https://doi.org/10.1021/acsnano.8b03365.
(17) Garaj, S.; Liu, S.; Golovchenko, J. A.; Branton, D. Molecule-Hugging Graphene Nanopores. *PNAS* **2013**, *110* (30), 12192–12196. https://doi.org/10.1073/pnas.1220012110.
(18) Merchant, C. A.; Healy, K.; Wanunu, M.; Ray, V.; Peterman, N.; Bartel, J.; Fischbein, M. D.; Venta, K.; Luo, Z.; Johnson, A. T. C.; et al. DNA Translocation through Graphene Nanopores. *Nano Lett.* **2010**, *10* (8), 2915–2921. https://doi.org/10.1021/nl101046t.
(19) Schneider, G. F.; Kowalczyk, S. W.; Calado, V. E.; Pandraud, G.; Zandbergen, H. W.; Vandersypen, L. M. K.; Dekker, C. DNA Translocation through Graphene Nanopores. *Nano Lett.* **2010**, *10* (8), 3163–3167. https://doi.org/10.1021/nl102069z.
(20) Tran, T. T.; Bray, K.; Ford, M. J.; Toth, M.; Aharonovich, I. Quantum Emission from Hexagonal Boron Nitride Monolayers. *Nature Nanotechnology* **2016**, *11* (1), 37–41. https://doi.org/10.1038/nnano.2015.242.
(21) Koenig, S. P.; Wang, L.; Pellegrino, J.; Bunch, J. S. Selective Molecular Sieving through Porous Graphene. *Nature Nanotechnology* **2012**, *7* (11), 728–732. https://doi.org/10.1038/nnano.2012.162.
(22) Zhao, J.; He, G.; Huang, S.; Villalobos, L. F.; Dakhchoune, M.; Bassas, H.; Agrawal, K. V. Etching Gas-Sieving Nanopores in Single-Layer Graphene with an Angstrom Precision for High-Performance Gas Mixture Separation. *Science Advances* **2019**, *5* (1), eaav1851. https://doi.org/10.1126/sciadv.aav1851.
(23) O'Hern, S. C.; Boutilier, M. S. H.; Idrobo, J.-C.; Song, Y.; Kong, J.; Laoui, T.; Atieh, M.; Karnik, R. Selective Ionic Transport through Tunable Subnanometer Pores in Single-Layer Graphene Membranes. *Nano Lett.* **2014**, *14* (3), 1234–1241. https://doi.org/10.1021/nl404118f.
(24) Heiranian, M.; Farimani, A. B.; Aluru, N. R. Water Desalination with a Single-Layer MoS 2 Nanopore. *Nature Communications* **2015**, *6* (1), 1–6. https://doi.org/10.1038/ncomms9616.
(25) Wang, L.; Drahushuk, L. W.; Cantley, L.; Koenig, S. P.; Liu, X.; Pellegrino, J.; Strano, M. S.; Bunch, J. S. Molecular Valves for Controlling Gas Phase Transport Made from Discrete Ångström-Sized Pores in Graphene. *Nature Nanotechnology* **2015**, *10* (9), 785–790. https://doi.org/10.1038/nnano.2015.158.
(26) Kidambi, P. R.; Jang, D.; Idrobo, J.-C.; Boutilier, M. S. H.; Wang, L.; Kong, J.; Karnik, R. Nanoporous Atomically Thin Graphene Membranes for Desalting and Dialysis Applications. *Advanced Materials* **2017**, *29* (33), 1700277. https://doi.org/10.1002/adma.201700277.
(27) Emmrich, D.; Beyer, A.; Nadzeyka, A.; Bauerdick, S.; Meyer, J. C.; Kotakoski, J.; Gölzhäuser, A. Nanopore Fabrication and Characterization by Helium Ion Microscopy. *Appl. Phys. Lett.* **2016**, *108* (16), 163103. https://doi.org/10.1063/1.4947277.
(28) Kotakoski, J.; Jin, C. H.; Lehtinen, O.; Suenaga, K.; Krasheninnikov, A. V. Electron Knock-on Damage in Hexagonal Boron Nitride Monolayers. *Phys. Rev. B* **2010**, *82* (11), 113404. https://doi.org/10.1103/PhysRevB.82.113404.
(29) Jin, C.; Lin, F.; Suenaga, K.; Iijima, S. Fabrication of a Freestanding Boron Nitride Single Layer and Its Defect Assignments. *Phys. Rev. Lett.* **2009**, *102* (19), 195505. https://doi.org/10.1103/PhysRevLett.102.195505.
(30) Warner, J. H.; Rümmeli, M. H.; Bachmatiuk, A.; Büchner, B. Atomic Resolution Imaging and Topography of Boron Nitride Sheets Produced by Chemical Exfoliation. *ACS Nano* **2010**, *4* (3), 1299–1304. https://doi.org/10.1021/nn901648q.
(31) Ryu, G. H.; Park, H. J.; Ryou, J.; Park, J.; Lee, J.; Kim, G.; Shin, H. S.; Bielawski, C. W.; Ruoff, R. S.; Hong, S.; et al. Atomic-Scale Dynamics of Triangular Hole Growth in Monolayer Hexagonal Boron Nitride under Electron Irradiation. *Nanoscale* **2015**, *7* (24), 10600–10605. https://doi.org/10.1039/C5NR01473E.

(32) Gilbert, S. M.; Dunn, G.; Azizi, A.; Pham, T.; Shevitski, B.; Dimitrov, E.; Liu, S.; Aloni, S.; Zettl, A. Fabrication of Subnanometer-Precision Nanopores in Hexagonal Boron Nitride. *Scientific Reports* **2017**, *7* (1), 15096. https://doi.org/10.1038/s41598-017-12684-x.
(33) Zobelli, A.; Gloter, A.; Ewels, C. P.; Seifert, G.; Colliex, C. Electron Knock-on Cross Section of Carbon and Boron Nitride Nanotubes. *Phys. Rev. B* **2007**, *75* (24), 245402. https://doi.org/10.1103/PhysRevB.75.245402.
(34) Pham, T.; Gibb, A. L.; Li, Z.; Gilbert, S. M.; Song, C.; Louie, S. G.; Zettl, A. Formation and Dynamics of Electron-Irradiation-Induced Defects in Hexagonal Boron Nitride at Elevated Temperatures. *Nano Lett.* **2016**, *16* (11), 7142–7147. https://doi.org/10.1021/acs.nanolett.6b03442.
(35) Gilbert, S. M.; Pham, T.; Dogan, M.; Oh, S.; Shevitski, B.; Schumm, G.; Liu, S.; Ercius, P.; Aloni, S.; Cohen, M. L.; et al. Alternative Stacking Sequences in Hexagonal Boron Nitride. *2D Mater.* **2019**, *6* (2), 021006. https://doi.org/10.1088/2053-1583/ab0e24.
(36) Zheng, F.; Zhou, G.; Liu, Z.; Wu, J.; Duan, W.; Gu, B.-L.; Zhang, S. B. Half Metallicity along the Edge of Zigzag Boron Nitride Nanoribbons. *Phys. Rev. B* **2008**, *78* (20), 205415. https://doi.org/10.1103/PhysRevB.78.205415.
(37) Du, A.; Chen, Y.; Zhu, Z.; Amal, R.; Lu, G. Q. (Max); Smith, S. C. Dots versus Antidots: Computational Exploration of Structure, Magnetism, and Half-Metallicity in Boron−Nitride Nanostructures. *J. Am. Chem. Soc.* **2009**, *131* (47), 17354–17359. https://doi.org/10.1021/ja9071942.
(38) Yin, L.-C.; Cheng, H.-M.; Saito, R. Triangle Defect States of Hexagonal Boron Nitride Atomic Layer: Density Functional Theory Calculations. *Phys. Rev. B* **2010**, *81* (15), 153407. https://doi.org/10.1103/PhysRevB.81.153407.
(39) Cretu, O.; Lin, Y.-C.; Koshino, M.; Tizei, L. H. G.; Liu, Z.; Suenaga, K. Structure and Local Chemical Properties of Boron-Terminated Tetravacancies in Hexagonal Boron Nitride. *Phys. Rev. Lett.* **2015**, *114* (7), 075502. https://doi.org/10.1103/PhysRevLett.114.075502.
(40) Ryou, J.; Park, J.; Hong, S. Investigations of Vacancy Structures Related to Their Growth in H-BN Sheet. *Nanoscale Research Letters* **2017**, *12* (1), 445. https://doi.org/10.1186/s11671-017-2194-6.
(41) Choi, S.; Tran, T. T.; Elbadawi, C.; Lobo, C.; Wang, X.; Juodkazis, S.; Seniutinas, G.; Toth, M.; Aharonovich, I. Engineering and Localization of Quantum Emitters in Large Hexagonal Boron Nitride Layers. *ACS Appl. Mater. Interfaces* **2016**, *8* (43), 29642–29648. https://doi.org/10.1021/acsami.6b09875.
(42) Barone, V.; Peralta, J. E. Magnetic Boron Nitride Nanoribbons with Tunable Electronic Properties. *Nano Lett.* **2008**, *8* (8), 2210–2214. https://doi.org/10.1021/nl080745j.
(43) Perdew, J. P.; Zunger, A. Self-Interaction Correction to Density-Functional Approximations for Many-Electron Systems. *Phys. Rev. B* **1981**, *23* (10), 5048–5079. https://doi.org/10.1103/PhysRevB.23.5048.
(44) Giannozzi, P.; Baroni, S.; Bonini, N.; Calandra, M.; Car, R.; Cavazzoni, C.; Davide Ceresoli; Chiarotti, G. L.; Cococcioni, M.; Dabo, I.; et al. QUANTUM ESPRESSO: A Modular and Open-Source Software Project for Quantum Simulations of Materials. *J. Phys.: Condens. Matter* **2009**, *21* (39), 395502. https://doi.org/10.1088/0953-8984/21/39/395502.
(45) Hamann, D. R. Optimized Norm-Conserving Vanderbilt Pseudopotentials. *Phys. Rev. B* **2013**, *88* (8), 085117. https://doi.org/10.1103/PhysRevB.88.085117.
(46) Grimme, S. Semiempirical GGA-type density functional constructed with a long-range dispersion correction. *Journal of Computational Chemistry* **2006**, *27* (15), 1787–1799. https://doi.org/10.1002/jcc.20495.